Soft Matter

Tuning Thin-film Bijels with Applied External Electric Fields

Journal:	*Soft Matter*
Manuscript ID	SM-ART-03-2018-000638.R1
Article Type:	Paper
Date Submitted by the Author:	01-May-2018
Complete List of Authors:	Carmack, Joseph; University of Arkansas, Mechanical Engineering Millett, Paul; University of Arkansas, Department of Mechanical Engineering

ARTICLE TYPE www. rsc.org/xxxxxx | XXXXXXXX

Tuning Thin-film Bijels with Applied External Electric Fields†

Joseph M. Carmack*[a] **and Paul C. Millett**[a]

Received Xth XXXXXXXXXX 20XX, Accepted Xth XXXXXXXXX 20XX
First published on the web Xth XXXXXXXXXX 200X
DOI: 10.1039/b000000x

The tunability of thin-film bijels using applied external electric fields is explored using a Cahn-Hilliard Langevin Dynamics computational model. Dielectric contrast between liquid domains governs liquid domain alignment and was varied in the simulations. Dielectric contrast between colloidal particles and liquid matrix induces dipolar particle interactions and was also varied in the simulations. The study reveals unique internal morphologies including those with through-thickness liquid domains. Significant results include identification of electric field effects on phase evolution and final morphology as well as relevant mechanisms. It was also found that particle chains act as nucleation sites for phase separation. The resultant morphologies were analyzed in terms of particle attachment to phase interface regions as well as the average channel diameter. Electric field effects and mechanisms on morphology are identified and compared with other morphology-tuning parameters such as particle loading and liquid-liquid composition.

1 Introduction

Bijels are a class of soft materials discovered fairly recently in 2005 [1,2]. The term bijel stands for "Bicontinuous Interfacially Jammed Emulsion Gel". Although their formation process is a topic of current research [3–5], it generally involves a system of two phase separating liquids, usually close to the critical composition, with the addition of colloidal particles. Processing routes typically involve quenching the system into the spinodal region thereby inducing phase separation via spinodal decomposition. This phase separation is eventually arrested by particle jamming at the interfaces between the two liquids. The colloidal particles must have fairly equal affinity for both liquids which results in a solid/liquid/liquid contact angle of approximately 90°. As phase separation proceeds, the particles form a dense monolayer on the interface and halt the separation process. The jammed liquid domains form a bicontinuous network where the average domain size, or separation distance between interfaces, is approximately constant. This property is similar to that of the geometric gyroid structure [6], however without long-range order. This jammed bicontinuous state is what is typically referred to as a bijel. In this work we will show how such morphologies in thin-film geometries can be drastically modified by the application of external electric fields to create aligned morphologies that retain colloidal particles attached to the liquid-liquid interfaces.

Bijels have many promising applications in the soft materials industry due to their unique properties and morphology tunability. Bijels have been used as template scaffolds [7] for creating many novel materials such as monolithic porous metals [8–10], battery electrodes [11], and cell delivery materials [12]. Most bijel studies, theoretical and experimental, have been performed in bulk conditions. Bijels confined to thin-films are a new area of research in this field with only a few studies having been completed [13–15]. The study of thin-film bijels is motivated by factors such as the potential for roll-to-roll processing, morphology diversity and tunability [15], and the creation of membranes with enhanced properties due to the interfacial nanoparticles.

The application of an electric field is known to align the domains of immiscible homopolymer blends [16,17] and block copolymers [18–20]. Furthermore, electric fields can assemble colloidal particles suspended in a solvent into 1D chains or 2D walls [21,22], depending on the particle volume fraction, with the classic example being an electrorheological fluid. The basic principle for either case is the difference between the dielectric properties of the two matrix phases, or between the particles and the matrix.

This work is focused on simulating the effects of applied external electric fields to thin-film bijels composed of viscous liquids, such as polymer solutions, and their morphology evolution from initial quench to a final jammed state. Although one might speculate that domain and particle alignment should occur, the true effect of the electric field on the structure of the bijel domains, or the structure of the particle-coated interfaces, is not known. For example, is it possible that an electric field of sufficient strength may detach particles from the interface? Previous studies have shown that interfacially-attached particles in oil-in-water droplets remain attached in electric

† Electronic Supplementary Information (ESI) available: [details of any supplementary information available should be included here]. See DOI: 10.1039/b000000x/

[a] Department of Mechanical Engineering, University of Arkansas, Fayetteville, AR 72701, USA. E-mail: pmillett@uark.edu

fields, which can elongate the droplets[23] or re-organize the particle arrangements[24]. Here, we have extended a Cahn-Hilliard Langevin Dynamics computational model developed in our previous work[13,15] to simulate applied electric fields to thin-film bijels.

2 Methods

2.1 Computational Model

The Cahn-Hilliard Langevin Dynamics computational model is composed of two sub-models which are then directly coupled. The first sub-model is a Cahn-Hilliard model which evolves a set of order parameters through space and time. For this work, there are three order parameters that are evolved on a Cartesian grid. Two of these order parameters, $\phi_1(x,y,z,t)$ and $\phi_2(x,y,z,t)$, represent the volume fraction for each constitutive liquid phase. The assumption of high viscosity is due to the fact that the Cahn-Hilliard equation models diffusion-based transport only and does not account for convective transport. The third order parameter, $\psi(x,y,z,t)$, represents the local presence of a solid particle. It is not evolved by the Cahn-Hilliard equation but is used in the coupling of the two sub-models which will be explained shortly. Additionally, the Cahn-Hilliard model is modified from its normal form by including a term to account for the effects of an applied external electric field.

The other sub-model is a Langevin particle dynamics model which evolves a suspension of solid colloids through space and time and is very similar to a classical molecular dynamics model. The Langevin dynamics model is also modified to simulate the Brownian motion of the particles in the presence of an electric-field.

2.2 Cahn-Hilliard model

The modified Cahn-Hilliard (CH) equation is given by:

$$\frac{\partial \phi_i}{\partial t} = M_i \nabla^2 \frac{\delta F}{\delta \phi_i} + k_z \frac{\partial^2 \phi_i}{\partial z^2} + \zeta \qquad (1)$$

where $i = 1,2$ yielding a set of CH equations for evolving each liquid volume fraction, $\phi_1(x,y,z,t)$ and $\phi_2(x,y,z,t)$, through space and time. In Eq. (1), M_i is a mobility term for liquid i and ζ is a small random fluctuation term that models thermal noise in the liquid order-parameter fields. The $k_z \frac{\partial^2 \phi_i}{\partial z^2}$ term is a modification that models the liquid domain alignment in the electric field direction (here, the z-direction)[25]. It models an electrostatic pressure on the interfaces by adding an energetic penalty for z-gradients in the ϕ_i parameters. k_z is proportional to the square of the electric field strength, E_0, and the square of the dielectric discrepancy between phases $(\varepsilon_1 - \varepsilon_2)$:

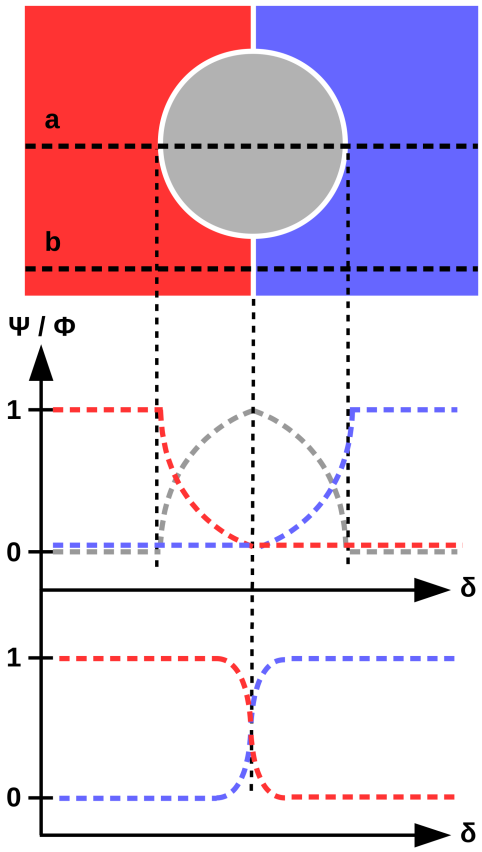

Fig. 1 (Top) Schematic showing two liquid domains (red and blue) with particle at the liquid-liquid interface (gray). (Middle) Plot showing the values of the order parameters ϕ_1, ϕ_2, and ψ and how they vary as you traverse the dotted line **a**. (Bottom) Plot showing the values of the order parameters ϕ_1 and ϕ_2 and how they vary as you traverse the dashed line **b**.

$$k_z = \frac{\varepsilon_0 v_0}{k_B T} \frac{2E_0^2 (\varepsilon_1 - \varepsilon_2)^2}{(\varepsilon_1 + \varepsilon_2)} \qquad (2)$$

where ε_0 is the permitivity of free space, v_0 is the volume of one monomer, E_0 is the strength of the electric field which is oriented in the z-direction or perpendicular to the film, and ε_1 and ε_2 are the dielectric constants of the two liquid phases. In typical experimental conditions for a polymer blend, for example PS/PMMA, a value of $k_z = 0.1$ corresponds to an electric field strength of $8V/\mu m$[26].

The free energy density F in Eq. (1) is given by:

$$F = \int [f(\phi_1, \phi_2, \psi) + \kappa(\nabla \phi_1)^2 + \kappa(\nabla \phi_2)^2] dV. \qquad (3)$$

where $f(\phi_1, \phi_2, \psi)$ is the bulk free energy density and the gradient terms account for the liquid-liquid interfacial energy. The κ parameter is a coefficient that scales the interfacial energy. The relationship between the three order parameters ϕ_1,

ϕ_2, and ψ are schematically represented in Fig. 1. The ψ order paramter is a mapping of the function in Eq. 4 to the local region of the grid occupied by each particle.

$$\psi_j(\mathbf{r}) = \begin{cases} 1 - \left(\frac{|\mathbf{r}-\mathbf{r}_j^{cm}|}{rad_j}\right)^2 & 0 \le |\mathbf{r}-\mathbf{r}_j^{cm}| \le rad_j \\ 0 & rad_j < |\mathbf{r}-\mathbf{r}_j^{cm}| \end{cases} \quad (4)$$

In Eq. 4, the vector $\mathbf{r}$ represents a location in the simulation domain, rad_j and $\mathbf{r}_j^{cm}$ are the radius and center-of-mass position vector of the j^{th} particle, and $\psi_j(\mathbf{r})$ is mapped for every single particle in the system.

The functional form of the bulk free energy density, $f(\phi_1, \phi_2, \psi)$ in Eq. (3) is a polynomial function of ϕ_1, ϕ_2, and ψ of the form:

$$f = w(f_{ll} + f_{lp}), \quad (5)$$

where:

$$f_{ll} = (3\phi_1^4 - 4\phi_1^3) + (3\phi_2^4 - 4\phi_2^3) + 6\phi_1^2\phi_2^2 \quad (6)$$

$$f_{lp} = 6\psi(\phi_1^2 + \phi_2^2) \quad (7)$$

f_{ll} accounts for liquid-liquid interactions, f_{lp} for liquid-particle interactions, and w is a scaling coefficient. f_{ll} is a double-well function with minima at $(\phi_1, \phi_2) = (1,0), (0,1)$ and a miscibility gap between the two minima which approximates the Flory-Huggins free energy density model for polymer solutions[27,28]. f_{lp} is only ever activated in regions of the simulation domain occupied by particles (i.e. where ψ is nonzero). This changes the free energy density model inside particles to have a single energy minima at $(\phi_1, \phi_2) = (0,0)$ which serves to drive both liquid species out of domains occupied by particles. An in-depth discussion of the model given in Eq. (3) is available in previous publications[14,15].

2.3 Langevin Dynamics model

The Langevin dynamics sub-model evolves a system of colloidal particles in space and time according to their equations of motion. The equation of motion for particle j is given by:

$$m_j \mathbf{a}_j = \mathbf{F}_j^{pp} - \mathbf{F}_j^d + \mathbf{F}_j^s + \mathbf{F}_j^c \quad (8)$$

where m_j and $\mathbf{a}_j$ are the mass and acceleration of particle j, and $\mathbf{F}_j^{pp}$, $\mathbf{F}_j^d$, $\mathbf{F}_j^s$, and $\mathbf{F}_j^c$ are the particle-particle interaction force, drag force, stochastic Brownian force, and capillary force exerted on particle j, respectively.

Particle-particle interactions forces have two main components. First there is a soft steric repulsion force calculated on particle j from particle i as:

$$\mathbf{F}_{ij}^{rep} = \sigma \left(\frac{2r_{avg}}{r_{ij}}\right)^n, \quad (9)$$

where r_{ij} is the center-to-center particle distance, r_{avg} is the average radius of particle i and j, σ is a constant used to scale the repulsive force strength, and n is an integer exponent ($n = 7$ for this work). The second component of the particle-particle interaction force is an electric-field induced dipole-dipole force. Using the point dipole approximation[29] it is calculated as:

$$\mathbf{F}_{ij}^{dip} = R_{dd}\left[\left(3cos^2\theta - 1\right)\hat{r} + (sin2\theta)\,\hat{\theta}\right] \quad (10)$$

$$R_{dd} = \frac{r_{avg}^6 C^2 E_0^2}{r_{ij}^4} \quad (11)$$

where $C = (\varepsilon_p - \varepsilon_m)/(\varepsilon_p + 2\varepsilon_m)$ is the particle polarizability or Clausius-Mossotti relation and θ is the angle between the particle separation vector $\mathbf{r}_{ij}$ and the direction of the electric field (here, the z-direction). In the Clausius-Mossotti relation, ε_p is the dielectric constant of the particle and ε_m is the dielectric constant of the liquid-liquid matrix in which the particle resides. $\hat{r}$ is the unit vector pointing in the direction of the separation vector of the two particles $\mathbf{r}_{ij}$, and $\hat{\theta}$ is the corresponding orthogonal unit vector pointing in the theta rotation direction.

The particle-particle interaction force on particle j in Eq. (8) is given as the sum of the steric repulsion forces and dipole-dipole interaction forces:

$$\mathbf{F}_j^{pp} = \sum_{i=1}^{nbrs}\left(\mathbf{F}_{ij}^{rep} + \mathbf{F}_{ij}^{dip}\right) \quad (12)$$

where the sum is over all the neighbor particles to particle j within a cutoff radius distance, r_{cut}.

The drag force on the j^{th} particle is calculated by:

$$\mathbf{F}_j^d = -\gamma \mathbf{v}_j \quad (13)$$

where γ is the drag coefficient, which is related to the viscosity of the liquid matrix in which the colloids are dispersed, and $\mathbf{v}_j$ is the velocity of particle j.

The stochastic or Brownian force is calculated using the following relation:

$$\mathbf{F}_j^s = \sqrt{2.0 \cdot \gamma \cdot \nu} \cdot \mathbf{R} \quad (14)$$

where ν is a parameter used to scale the Brownian motion strength and is related to temperature. $\mathbf{R}$ is a vector with each xyz component drawn from a uniform random distribution over the interval $[-1, 1]$.

The capillary force on the j^{th} particle is calculated using order parameter information from the Cartesian grid:

$$\mathbf{F}_j^c = D\sum_k\sum_l\sum_m \psi_j^{klm}\phi_1^{klm}\phi_2^{klm}\left(\mathbf{r}_{klm} - \mathbf{r}_j^{cm}\right) \quad (15)$$

D is a force constant used to scale the capillary force and the triple summation is over the local section of the grid occupied

by particle j. $\mathbf{r}_j^{cm}$ is the center-of-mass position vector of particle j, $\mathbf{r}_{klm}$ is the position vector of the local grid node, and ψ_j^{klm}, ϕ_1^{klm}, and ϕ_2^{klm} are the values of the order parameters at the local node. This form of the capillary force calculation ensures that capillary forces are only non-zero when located at liquid-liquid interfaces and has been validated to produce correct capillary forces for spherical particles[13].

2.4 Coupling of Cahn-Hilliard and Langevin Dynamics Submodels

In both the sub-models described above, surface tension or interfacial energy is the key parameter linking the two models. In the Cahn-Hilliard sub-model the interfacial energy between liquids ϕ_1 and ϕ_2 is non-linearly proportional to the product of w in Eq. (5) and κ in Eq. (3):

$$\sigma_{12} \sim \sqrt{w \cdot \kappa} \tag{16}$$

Thus, for example, by increasing the surface tension in the model by increasing w or κ, the energy barrier for nucleation of a minority phase in a highly off critical composition would increase.

In the Langevin Dynamics sub-model the capillary forces on particles are directly proportional to the surface tension between the two liquids. Thus the scaling factor D in Eq. (15) represents the influence of surface tension on particles. Thus by increasing the value of D in our model, the particles experience stronger capillary forces due to increased surface tension. The way that particles induce jamming of liquid-liquid phase separation in the Cahn-Hilliard sub-model is by literally covering up or removing liquid-liquid interface. This is facilitated when liquids are expelled from regions occupied by particles which is induced by the f_{lp} term of Eq. (5).

2.5 Length and Time Scales

There are two primary time scales for the computational model: one associated with the Brownian motion of the colloids which we denote τ_{part} and the other associated with the diffusion based transport of polymers species which we denote as τ_{pol}. By assuming a size for colloidal particles, the Brownian motion time scale can be estimated using the Stokes-Einstien relation $\tau_{part} = 6\pi\eta_m r_p^3/k_bT$, where η_m is the viscosity of the suspension matrix, r_p is the radius of the colliods, k_b is Boltzmann's constant, and T is the absolute temperature. An estimate for the time scale for phase separation kinetics can be calculated using $\tau_{pol} \approx (2r_p)^2/D_{pol}$, where D_{pol} is the mutual diffusion coefficient of the liquids. For a system of PS/PMMA in a semidilute solution and dispersion of Silica nanoparticles, typical parameters such as absolute temperature $T \approx 300\ K$, average polymer molecular weight $M_w \sim 10^2\ kg \cdot mol^{-1}$, matrix viscosity $\eta_m \sim 10^{-2}\ Pa \cdot s$[30–32], average polymer diffusion coefficient $D_{pol} \sim 10^{-7}\ cm^2 \cdot s^{-1}$[31–33], and nanoparticle diameters of 200 nm, results in $\tau_{pol} \sim 10^{-3}\ s$ and $\tau_{part} \sim 10^{-2}\ s$. Using a time step $\Delta t = 0.1\tau_{pol}$ for a simulation consisting of 1.5×10^6 steps correlates to a simulation time on the order of 2 min for the sample parameters given. Parameters for a polymer melt system can be substituted in the above equations to estimate simulation times for polymer melt experiments; however, it should be noted that for polymer melts the Stokes-Einstien relation can significantly over estimate the Brownian motion time scale[31,32]. The length scales of the simulation are set by the assumed nanoparticle sizes. In our simulations, particle diameters are typically $6\delta - 10\delta$ grid nodes in length. The simulation domain is discretized into a cartesion grid with uniform node spacing denoted as δ and has a value of $\delta = 1.0$ for all the simulations. For an assumed particle diameter of 200 nm used in the above example, δ corresponds to a length of about $20 - 30\ nm$. This results in simulation domain sizes of roughly $5\ \mu m \times 5\mu m \times 2\mu m$ for the $x \times y \times z$ dimensions.

2.6 Simulation Setup and Numerical Solution Scheme

Each simulation evolves a system of immiscible liquids with a suspension of colloidal particles from an initial homogeneous state with some liquid/liquid composition (ϕ_1, ϕ_2) and particle loading (ϕ_p). The start of each simulation corresponds to an instantaneous thermal quench below the binodal curve, and the system is then evolved for a specified number of simulation steps.

The coupled Cahn-Hilliard Langevin Dynamics model is implemented in the Meso simulation code[34] developed in our group. The code is parallelized to run on modern supercomputer clusters to allow large simulations to be run in practical amounts of time. The Cahn-Hilliard sub-model is numerically integrated using a semi-implicit spectral method[35] that utilizes the FFTw implementation of the Fourier transform[36]. The Langevin Dynamics sub-model uses a standard velocity-verlet algorithm to numerically integrate the equations of motion. Boundary conditions for both the Cahn-Hilliard and Langevin Dynamics sub-models are periodic in the thin-film's lateral dimensions (x- and y-directions). At the z-boundaries (top and bottom of the film), a no-flux boundary is implemented by imposing single layers of solid material with $\psi = 1.0$.

For all simulations, particle positions are initialized randomly throughout the domain or, in cases with larger particle loading, on a cubic lattice with random displacements. This is followed by an equilibration run where the only active forces are the soft steric repulsions between particles and stochastic Brownian forces. This allows particles to settle into an initial state which is physically realistic. Following particle equilibration, the liquid domains are initialized about a chosen com-

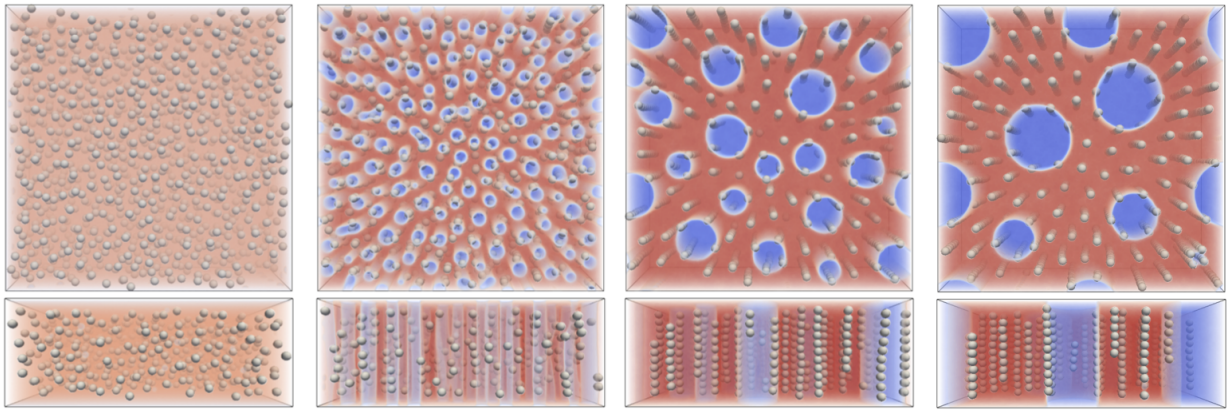

Fig. 2 Top down and side-view snapshots showing time evolution of the multi-phase morphology. From left to right, corresponding time stamps in terms of number of simulation steps taken are: 0 (initial condition), 380,000, 750,000, and 1,500,000 steps. Liquid domains are rendered as red (majority phase) and blue (minority phase) semitransparent volumes and interfaces rendered white. Colloidal particles are rendered as white spheres. The simulated thin film has a 65/35 fluid composition, a mesh size of $256 \times 256 \times 96$ in the xyz-dimensions, $C = k_z = 0.8$, particle volume fraction of 5.0% and particle diameter of $d_p = 8.0\delta$ where δ is the grid spacing.

position with small amounts of random noise. From this initial state, the simulation is launched. Since $\tau_{part}/\tau_{pol} \sim 10^1$, particle positions are updated after every 5 Cahn-Hilliard updates (our choice of 5 reflects simply the larger time scale of particles versus polymers, which are general approximations). Also, the applied external electric field is a constant, uniform DC field in the z-direction throughout the simulation domain for the duration of the entire simulation.

For each unique set of simulation parameters, three separate simulation runs were made to allow for the collection of statistics. For a list of all simulation parameters, see the supplementary information †. Several analysis tools were implemented to characterize the structures. Particle attachment at liquid-liquid interfaces was determined by looping over regions of the grid that particles occupy and searching for the existence of triple junctions between the liquids and particle (i.e. where $\phi_1, \phi_2 > 0.5$ and $\psi > 0.1$). The Hoshen-Kopelman algorithm[37] is used to calculate the number of liquid domains and their average size.

3 Simulation Results

We performed several parametric studies by independently varying the particle polarizability parameter C (see Eq. 10), the liquid-liquid dielectric contrast parameter k_z (see Eq. 1), the particle loading, and the liquid-liquid composition. Note that k_z and the dipole force $\mathbf{F}_j^d$ have the same dependence on the electric-field strength E_0, which means that varying the electric-field strength changes k_z and $\mathbf{F}_j^d$ in the same way. Consequently, by varying k_z and C in the model, we are effectively varying the dielectric contrast between liquid phases, $(\varepsilon_1 - \varepsilon_2)^2/(\varepsilon_1 + \varepsilon_2)$, and the dielectric contrast between particles and liquid matrix, $\left(\frac{\varepsilon_p - \varepsilon_m}{\varepsilon_p + 2\varepsilon_m}\right)^2$.

Simulations with values for k_z and C in the ranges $k_z = [0,1]$ and $C = [0,1]$ with varying film dimensions and particle sizes were run. Fig. 2 shows a sequence of renderings of the time evolution of a thin film with $C = k_z = 0.8$. The binary liquid mixture has a composition of 65/35 (ϕ_1/ϕ_2) and particle loading of $\phi_p = 5.0\%$. At the start of the simulation the system is very homogeneous and there are no interfaces. Also, particles are randomly and homogeneously distributed throughout the film. As time progresses, phase separation initiates and alignment of the phase domains in the electric-field direction occurs. The effect of the electric field transforms the three-dimensional bicontinuous morphology to that of a two-dimensional discrete morphology with through-thickness channels.

Particles also form chain-like structures due to their induced dipole-dipole interactions. Most of these chains become attached to the channel (phase) interfaces early on in the simulation. Throughout time, the channels coarsen due to Ostwald ripening. This corresponds to the shrinkage and disappearance of small channels, which feed the growth of larger channels. During this process, particle chains that exist on the interfaces can be swept along with the motion of the interface. Furthermore, the presence of particle chains on the channel interfaces can stabilize small channels and prevent them from dissolving. However, it seems that a certain number of particle chains is required to prevent the dissolution of a shrinking channel. Based on observation, this critical number of chains seems to be four, as evidenced by the disappearance of many

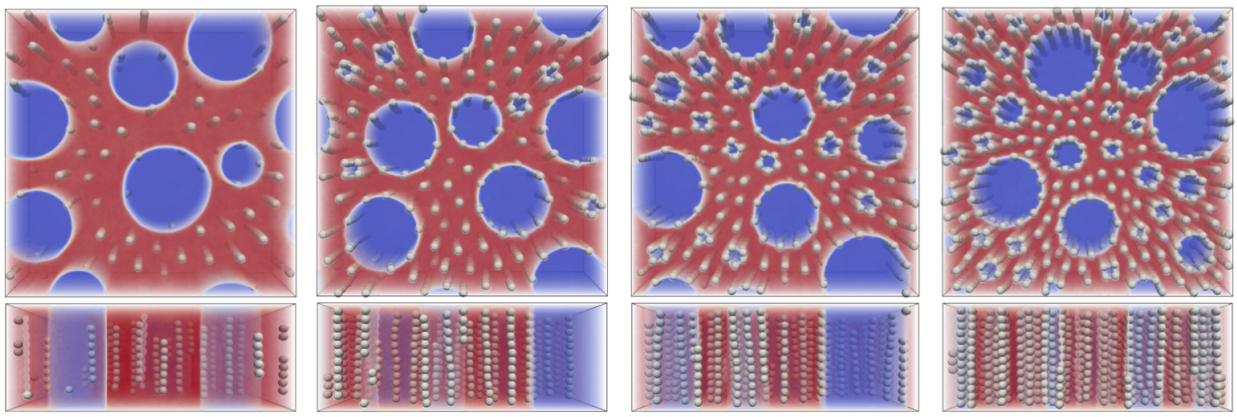

Fig. 3 Stabilized morphologies with through-thickness channels and varying degrees of particle loading. From left to right, the systems have ϕ_p values of 2.1%, 6.5%, 9.7%, and 15.0%. Each system has a 65/35 composition, a mesh size of $256 \times 256 \times 96$ in the xyz-dimensions, $C = k_z = 0.8$, and particle diameter $d_p = 8.0\delta$ where δ is the grid spacing.

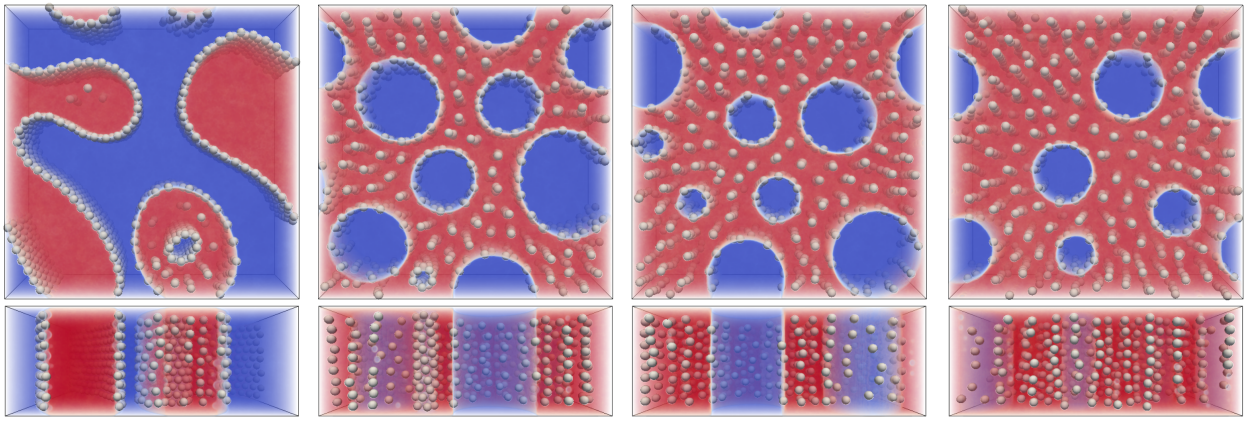

Fig. 4 Stabilized morphologies with through-thickness channels and varying composition. From left to right, the systems have 50/50, 60/40, 70/30, and 80/20 compositions, particle loading of $\phi_p = 5.0\%$, and a mesh size of $256 \times 256 \times 96$ in the xyz-dimensions, $C = k_z = 0.8$, and particle diameter $d_p = 8.0\delta$ where δ is the grid spacing.

channels with only three full chains attached and the continual existence of channels with four or more attached chains (see supplemental movie 1 †).

The number of chains required to stabilize a channel is a function of particle size. We saw evidence of this in simulations with smaller particle diameters ($d_p = 6\delta$) which required five particle chains to stabilize channels. In simulations with larger particles ($d_p = 10\delta$), we did not observe stabilized channels with three particle chains but suspect that this is due to the fact that $d_p = 8\delta - 10\delta$ is not quite large enough to stabilize channels with only three particle chains. We predict that increasing the particle size further would eventually result in channels stabilized by only three particle chains. The mechanism for this particle size dependence is the capillary force's variance with particle size. The size dependence of the capillary force defined in Eq. (15) comes from the fact that the magnitude of the vector difference $\mathbf{r}_{klm} - \mathbf{r}_j^{cm}$ increases with increasing particle diameter. We also expect channels stabilized by only three particle chains to be the lower limit of this effect; in other words, we believe it to be impossible to stabilize channels with only two particle chains.

Fig. 3 shows views of several film morphologies with different degrees of particle loading. Each simulation was run for the same number of simulation steps (1.5 million steps). Particle loading ranges from 2.1%-15.0% particle volume fractions. The necessary time to reach a fully jammed state is a function of particle loading. Note that the system with the smallest particle loading (ϕ_p = 2.1%) has larger channels which are not fully loaded with particle chains. This system has not reached a fully jammed state. With increasing ϕ_p, a

greater number of particle chains are attached to channel interfaces. The systems with the two highest particle loadings have fully jammed channel interfaces. Another interesting observation is the nature of the distribution of channel sizes. Morphologies that have not yet reached steady state have more unimodal distributions of channel sizes. Those that have reached a fully jammed state have more of a bimodal distribution of channel sizes. This seems to be due to the prevention of small-channel disappearance by the existence of four or more particle chains. Hence, the system exhibits a large number of small channels, and a few larger channels, with a distribution differing from that occurring during traditional Ostwald ripening.

Fig. 4 shows renderings of several morphologies with different liquid/liquid compositions. As was the case for varying particle loading, each simulation was run for the same number of simulation steps (1.5 million steps). Going left-to-right in Fig. (4), systems have compositions of 50/50, 60/40, 70/30, and 80/20. For the 50/50 composition, the morphology is two-dimensional but remains largely bicontinuous in the lateral dimensions. For compositions of 60/40 and up, the morphology is discrete with through-thickness channels and particle chains on the channel interfaces.

In addition, we ran simulations with a composition of 90/10, which generally will not exhibit phase separation due to a large nucleation barrier. However, we found that particle chaining can actually induce heterogenous nucleation of the minority phase, as shown in Fig. 5. Two simulations are shown, both with 90/10 composition, with one in which particle chaining occurs (due to dipole-dipole interactions), and one where particle chaining does not occur. Phase nucleation is observed when vertical particle chains begin forming, as shown in Fig. 5c, d (also, see supplemental movie 2 †). The aligned particle chains cause perturbations in the liquid concentration fields that favor nucleation events.

The above results illustrate the effect of varying levels of particle loading and fluid/fluid composition in electric-field aligned bijel films. These results all kept constant the influence of the electric field (constant values of $C = k_z = 0.8$). Varying the parameters associated with the electric field can significantly alter the film morphology. Fig. 6 shows the four typical morphologies that emerge when varying k_z and C (note: for clarity, only particles attached to interfaces are rendered). These morphologies represent the extreme points in the two-dimensional k_z/C parameter space. Fig. 6a is the stabilized morphology that evolves for weak particle polarizability and weak dielectric contrast between liquids (i.e. $k_z = C = 0.001$). It has large bicontinuous domains with densily coated particle interfaces, and the particles do not form chains. Fig. 6b is the case for weak particle polarizability and strong dielectric contrast between liquid phases (i.e. $k_z = 1.0$, $C = 0.001$). The morphology is discrete with through-thickness channels that are also densly covered with

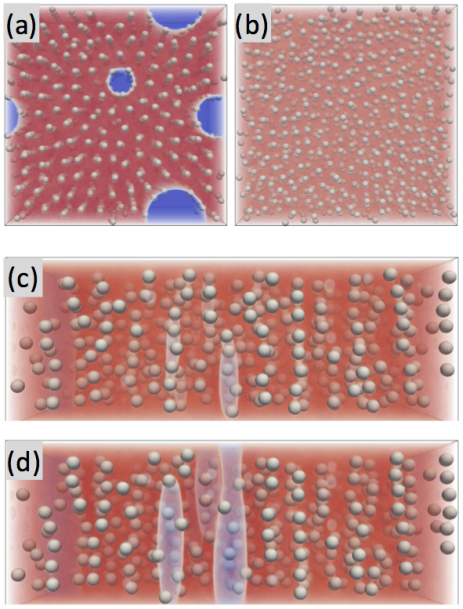

Fig. 5 a)-b) Top-dow views of two simulations, each with a 90/10 composition and $\phi_p = 5.0\%$. **a)** shows a film with strong particle polarizability $C = 0.5$ with particle chains and nucleated channels. **b)** show a film with weak particle polarizability $C = 0.05$ with no particle chaining and no nucleation process. **c)** and **d)** are side views of the system shown in **a)** at early simulation times (50,000 steps and 60,000 steps) which illustrate three nucleation events occurring at particle chain sites.

particles. Fig. 6c is the case of strong particle polarizability and weak dielectric contrast between liquids (i.e. $k_z = 0.001$, $C = 1.0$). The morphology is similar to that in Fig. 6a with the exception that all particles form chains, several of which have influenced the formation of channel-like structures. Despite this, discrete through-thickness channels have not formed as in the morphology in Fig. 6b. Finally, in Fig. 6d we have the case of strong particle polarizability and strong dielectric contrast between liquids (i.e. $k_z = C = 1.0$). The morphology is very similar to that in Fig. 6b except that particles have formed chains, and consequently their arrangement on the interface is different. Notice there are more stabilized channels in this morphology compared to the one in Fig. 6b.

4 Analysis and Discussion

From the morphologies shown in Fig. 6, it seems that in order for channels to form, the dielectric contrast between liquid phases must be higher than some threshold value. This is true no matter the strength of particle polarizability (at least in the ranges we studied). This being the case, we studied varying strengths of particle polarizability and its effect on channel

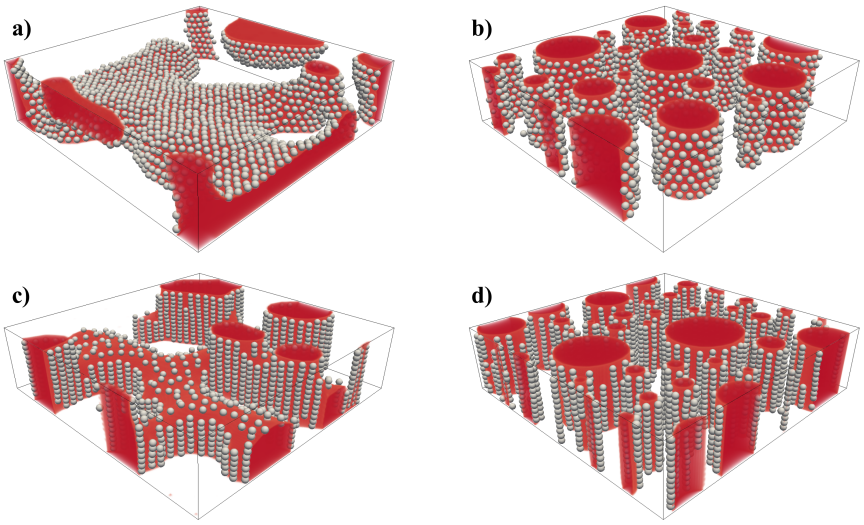

Fig. 6 Four basic morphologies found at the C and k_z parameter space extremes. **a)** corresponds to $C = 0.001$, $k_z = 0.001$, **b)** to $C = 0.001$, $k_z = 1.0$, **c)** to $C = 1.0$, $k_z = 0.001$, and **d)** to $C = 1.0$, $k_z = 0.001$. The composition is 65/35 for all morphologies. The minority phase is rendered as a semitransparent red volume and particles as solid white spheres. For clarity, only particles attached to the interfaces are rendered. Each system has a mesh size of $256 \times 256 \times 64$ in the xyz-dimensions, as well as a $\phi_p = 12.7\%$ with particle diameter $d_p = 6.0\delta$ where δ is the grid spacing.

formation and channel size for films with fixed particle loading $\phi_p = 12.7\%$ and liquid composition 65/35. We considered values of polarizability $C = 0.1, 0.3, 0.6, 0.9$ for two values of dielectric contrast between liquids, $k_z = 0.1, 0.9$. $k_z = 0.1$ corresponds to a slow rate of liquid domain alignment (which is still above the threshold), and $k_z = 0.9$ corresponds to a fast rate of liquid domain alignment. For $k_z = 0.9$, all domains align with the electric field within the first 5,000 simulation steps τ (simulation steps = simulation time/dt where dt is the time step). For $k_z = 0.1$, all domains reach full alignment by about 100,000 simulation steps. Before full alignment occurs, the morphology is a mixture of both through-thickness domains and unaligned domains. Eventually, however, with these parameters the morphologies all evolve into discrete through-thickness channels due to the electric field. We now investigate how the average channel diameter depends on the various material parameters specified in the model.

Fig. 7 shows the time evolution of the average channel diameter (ACD) for varying values of k_z and C. This data was calculated using the Hoshen-Kopelman algorithm[37]. For slow liquid domain alignment ($k_z = 0.1$), varying the strength of particle polarizability does not have a statistically significant effect on the ACD (left plot in Fig. 7). In contrast, for fast liquid domain alignment, it does (right plot in Fig. 7). This is because fast liquid domain alignment creates many smaller-sized channels early on which can then be stabilized by particles. However, the very small channels will only stabilize if there are also strong dipolar particle interactions, causing the formation of dense particle chains, which enhance the stabilization of small channels.

Fig. 8 shows the fraction of particles attached to liquid/liquid interfaces through time for the same conditions as Fig. 7. These plots clearly indicate the dependence of particle attachment on the strength of particle polarizability C. As the particle polarizability strength increases so does the fraction of particles attached to interfaces for both slow and fast liquid domain alignment; however, the effect is more pronounced for fast liquid domain alignment. This is due to the coupled effect of small diameter channels forming early on and becoming stabilized by tightly packed particle chains. Stronger dipolar interactions between particles also makes it harder for particles to be detached from channels shrinking due to Ostwald ripening because particles now experience a significant attractive force to one another. Particle chains also have a weak attraction to other chains that can allow them to form walls[21,22]; however, in our simulations the capillary forces and Brownian forces overshadow this effect.

We also investigated how the ACD varied with liquid/liquid composition. Fig. 9 shows the time evolution of ACD for five films with varying compositions (left plot) and their final ACD values at the end of the simulations (right plot). Here, the electric-field parameters have values of $k_z = 0.8$, $C = 0.8$. The range of stabilized ACD values in Fig. 9 has a size of about 10δ. This is about the same variation for the range of ACD values as that in Fig. 7.

Varying the particle loading has a much stronger effect on

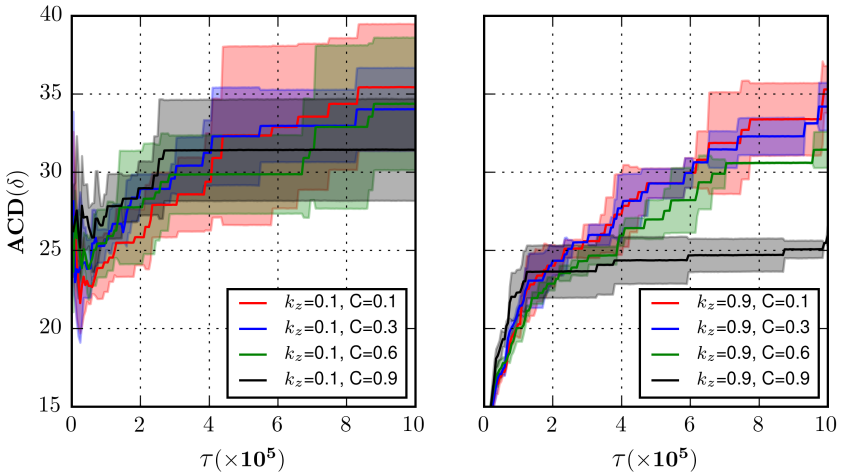

Fig. 7 Average channel diameter as a function of simulation steps τ. Each curve corresponds to the average value of three simulations with identical parameters, but different random initializations. The shaded regions about each curve show the standard deviation of the runs. Each simulation had a 65/35 composition, particle loading of $\phi_p = 12.7\%$, and a mesh size of $128 \times 128 \times 64$ in the xyz-dimensions, and particle diameter of $d_p = 6.0\delta$.

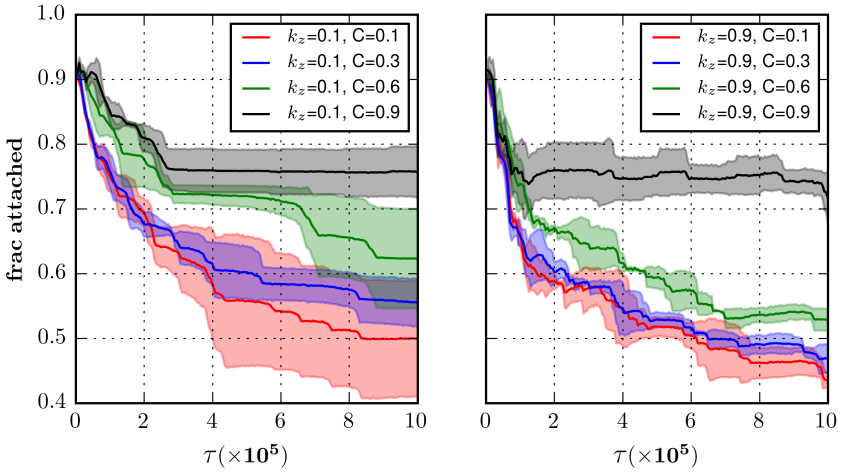

Fig. 8 Fraction of particles attached to liquid-liquid interfaces as a function of simulation steps τ. Each simulation had a 65/35 composition, particle loading of $\phi_p = 12.7\%$, and a mesh size of $128 \times 128 \times 64$ in the xyz-dimensions, and particle diameter of $d_p = 6.0\delta$.

the ACD than the liquid-liquid composition or electric properties of the system. Fig. 10 (left plot) shows the time evolution of ACD for a variety of films with varying degrees of particle loading (including the structures shown in Fig. (3)). The final stabilized ACD values are shown in the right plot. The range of ACD values produced by varying the particle loading is much larger than that produced by varying either the liquid-liquid composition or the electric properties of the system, with a variation of about 30δ. Each of these three main parameters (particle loading, composition, and electric properties of the system), can be considered as tuning nobs that have different strengths in their effect on channel sizes in these thin-film, particle-stabilizied emulsions.

5 Experimental Application

Most bijels have been experimentally fabricated using low molecular weight polar and non-polar mixtuers (oil and water based)[38]. A few studies have used higher molecular weight liquids such as polymer melts or two non-polar oligomers[39–41]. Due to our simulations only capturing dif-

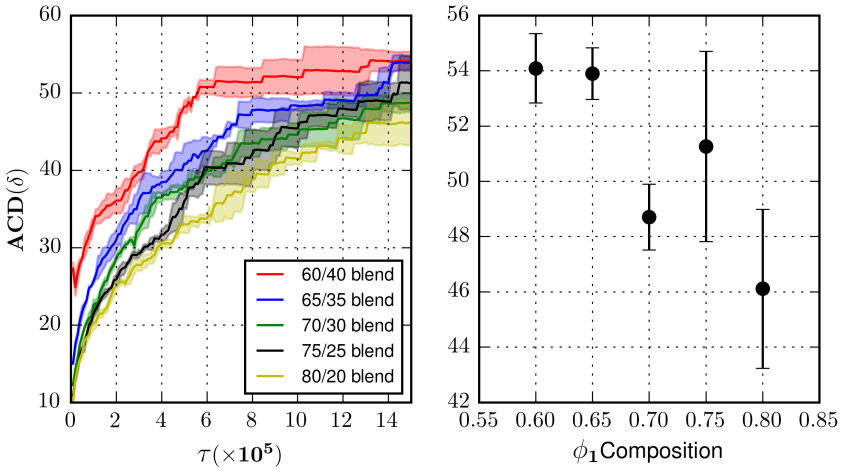

Fig. 9 Average channel diameter as a function of simulation steps τ (left) and composition in terms of ϕ_1 (right). The right plot shows the average channel diameter for each curve in the left plot at the final simulation step. Each simulation had a particle loading of $\phi_p = 5.0\%$, a mesh size of $256 \times 256 \times 96$ in the xyz-dimensions, particle diameter of $d_p = 8.0\delta$, and $C = k_z = 0.8$.

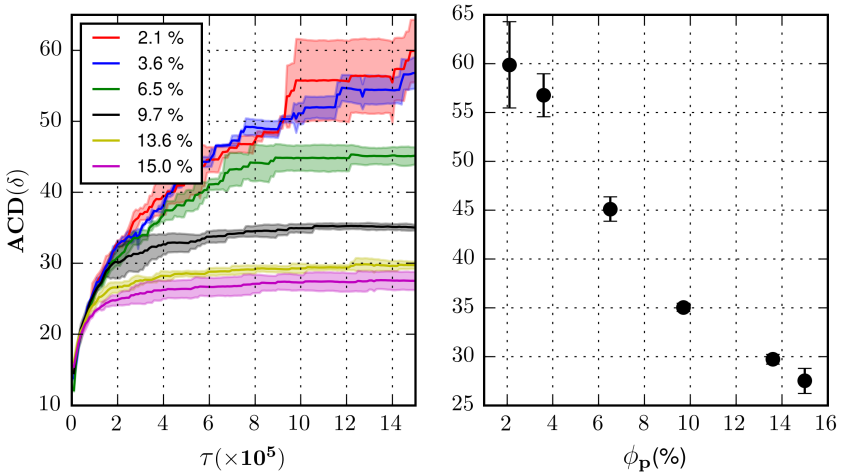

Fig. 10 Average channel diameter as a function of simulation steps τ (left) and particle loading ϕ_p (right). The right plot shows the average channel diameter for each curve in the left plot at the final simulation step. Each film in these simulations had a 65/35 composition, a mesh size of $256 \times 256 \times 96$ in the xyz-dimensions, particle diameter of $d_p = 8.0\delta$, and $C = k_z = 0.8$

fusion based liquid and particle transport, they best describe systems with higher viscosity liquid mixtures such as semidilute polymer solutions or polymer melts. In terms of electric fields, experiments have been done in which nanoparticles have been aligned in polymer solutions and melts[42–46]; however, to the best of the Authors' knowledge, no experiments of polymer bijels in the presence of electric fields have been published. We hope these simulation results will inspire experimental investigation into bijel systems fabricated from partially to fully immiscible polymer solutions or melts with nanoparticle suspensions in the presence of AC electric fields. Model experimental systems would need to have two different polymer species having low and high dielectric contrast correlating to the low and high k_z values of the simulations. Likewise, at least two different kinds of colloidal nanoparticles would need to be used, one with a dielectric constant similar to the average polymer species dielectric constant and one much higher. These would correlate to the low and high particle polarizabilities modeled in our simulations. Binary polymer systems and colloidal nanoparticles that fit these descriptions include PS/PMMA ($\varepsilon_{PMMA} - \varepsilon_{PS} \approx 1$), PS/Polybutadiene ($\varepsilon_{PB} - \varepsilon_{PS} \approx 0$), and Silica ($\varepsilon_{Si} \approx 3.8$)[47] and

Barium Titinate ($\varepsilon_{BT} \approx 2000$)[46,48] nanoparticles. These two polymer sytems and two nanoparticle types could be combined to create four unique thin-film polymer bijel systems. We hypothesize that the four resulting morphologies would qualitatively match those of our simulations presented in Fig. 6. Additionally, the main reason we suggest using AC versus DC electric fields in experiments is that use of DC electric fields is known to result in drifting of particles to one-side of the film due to an electrophoretic force caused by inhomogeneity in the DC field[42,46]. This unwanted field gradient effect can be negated in experiments by using high frequency AC fields which approximate the same effect as the idealized DC fields assumed in our simulations. Other experiments also reported faster and more uniform particle alignment using AC vs DC electric fields[43,45]. Furthermore, the nanoparticles would need to be surface treated to ensure they segregate to the polymer-polymer interfaces as has been done in previous experiments[39,40,49].

To ensure polymer domain alignment in experiments, the Clausius-Mossotti relation suggests the use of an AC field with high E_{RMS} but still below strengths that result in dielectric breakdown of the polymers. Previous experiments on electric field alignment of polymers can be used as guides for making initial estimates on what field strengths fit this criteria such as these experimental works[16–18,46,50–53]. Lastly, we would also expect the simulations to correlate to films with thicknesses on the order of 20-100 particle diameters. For nanoparticles with diameters in the range of 10-500 *nm* which have been used in previous thin-film polymer nanocomposit experiments[39,40,46], estimates of film thicknesses would be in the range of 1-50 μm. Also worth noting is that simulations presented here do not acount for surface wetting as was included in our previous simulations[14,15]. This was was done in order to isolate the effects of electric fields on the thin-film bijel morphology; consequently, we would expect experiments to see some effect from surface wetting on the thin-film morphology. In future research we expect to explore the combined effects of surface wetting and AC and DC electric fields using our computational bijel model.

6 Summary

To summarize, we have presented a simulation study of the effects of applied external electric fields on bijel morphology in thin films. The model captures the coupled effects of electric field alignment of liquid domains and dipole-dipole interactions of suspended particles that lead to chain formation. The rate of liquid domain alignment is controlled by the strength of the dielectric contrast between the two liquid phases. For slow rates of alignment, the morphology starts out bicontinuous and is transformed into a discrete morphology with through-thickness channels during the early stages of phase separation. During these early stages, phase separation is mediated by coalescence. It then changes to Ostwald ripening once the morphology is completely composed of discrete channels. For fast rates of alignment, the morphology is discrete with many small-diameter channels forming very early in the simulations. At these very early times, while channels are very small, phase separation proceeds via a mixture of channel coalescence and Ostwald ripening.

Despite the alignment of particles into chains by the electric field, it was found that unless a sufficient dielectric discrepancy between the liquid phases exists, through-thickness channels will not form. When channels do form, the strength of particle dipolar interactions has a strong effect on the organization of particles on the channel interfaces. With weak dipolar interaction, particles do not form chains and organize into two-dimensional close-packed monolayers on the interfaces. With strong dipolar particle interactions, particles form dense chains that promote channel jamming at smaller channel diameters due to the attractive dipolar forces between particles. Once a threshold value of particle chains are attached to a channel's interface, the channel will persist indefinitely. Furthermore, it was also found that particle chains act as nucleation sites for phase-separation.

Varying the dielectric contrast between liquids and the particle polarizability influences the average channel diameter to a similar degree as varying the liquid-liquid composition. The impact of varying particle loading on average channel diameter, however, is much stronger. This illustrates the coarse-to-fine tuning of channel sizes that can be accomplished using these parameters. The potential to tune these thin-film systems, their bottom-up assembly process, and their amenability to large-scale processing techniques (such as roll-to-roll processing) make them attractive candidates for creating new functional membranes.

7 Acknowledgments

The authors acknowledge support from the National Science Foundation under award No. CBET-1511896. JMC acknowledges support from the Doctoral Academy Fellowship provided by the University of Arkansas. This research is also supported by the Arkansas High Performance Computing Center which is funded through multiple National Science Foundation grants and the Arkansas Economic Development Commission.

References

1 K. Stratford, *Science*, 2005, **309**, 2198–2201.
2 M. E. Cates and P. S. Clegg, *Soft Matter*, 2008, **4**, 2132.
3 M. F. Haase, K. J. Stebe and D. Lee, *Advanced Materials*, 2015, **27**, 7065–7071.

4 C. Huang, J. Forth, W. Wang, K. Hong, G. S. Smith, B. A. Helms and T. P. Russell, *Nature nanotechnology*, 2017, **12**, 1060.

5 D. Cai, P. S. Clegg, T. Li, K. A. Rumble and J. W. Tavacoli, *Soft matter*, 2017, **13**, 4824–4829.

6 A. H. Schoen, *Infinite periodic minimal surfaces without self-intersections*, NASA Technical Report NASA TN D-5541, 1970.

7 M. N. Lee and A. Mohraz, *Advanced Materials*, 2010, **22**, 4836–4841.

8 M. N. Lee, M. A. Santiago-Cordoba, C. E. Hamilton, N. K. Subbaiyan, J. G. Duque and K. A. Obrey, *The journal of physical chemistry letters*, 2014, **5**, 809–812.

9 M. N. Lee and A. Mohraz, *Journal of the American Chemical Society*, 2011, **133**, 6945–6947.

10 M. N. Lee, J. H. Thijssen, J. A. Witt, P. S. Clegg and A. Mohraz, *Advanced Functional Materials*, 2013, **23**, 417–423.

11 J. Witt, D. Mumm and A. Mohraz, *Journal of Materials Chemistry A*, 2016, **4**, 1000–1007.

12 T. Thorson, E. Botvinick and A. Mohraz, *ACS Biomaterials Science & Engineering*, 2018.

13 P. C. Millett, *The Journal of chemical physics*, 2014, **140**, 144903.

14 J. M. Carmack and P. C. Millett, *The Journal of chemical physics*, 2015, **143**, 154701.

15 J. M. Carmack and P. C. Millett, *Soft matter*, 2017, **13**, 4214–4223.

16 H. Hori, O. Urakawa, O. Yano and Q. Tran-Cong-Miyata, *Macromolecules*, 2007, **40**, 389–394.

17 E. SchaÈffer, T. Thurn-Albrecht, T. P. Russell and U. Steiner, *Nature*, 2000, **403**, 874.

18 V. Olszowka, M. Hund, V. Kuntermann, S. Scherdel, L. Tsarkova, A. Böker and G. Krausch, *Soft Matter*, 2006, **2**, 1089–1094.

19 S. Elhadj, J. Woody, V. Niu and R. Saraf, *Applied physics letters*, 2003, **82**, 871–873.

20 T. Thurn-Albrecht, J. DeRouchey, T. Russell and H. Jaeger, *Macromolecules*, 2000, **33**, 3250–3253.

21 A. K. Agarwal and A. Yethiraj, *Physical review letters*, 2009, **102**, 198301.

22 J. S. Park and D. Saintillan, *Physical Review E*, 2011, **83**, 041409.

23 M. Cui, T. Emrick and T. P. Russell, *Science*, 2013, **342**, 460–463.

24 P. Dommersnes, Z. Rozynek, A. Mikkelsen, R. Castberg, K. Kjerstad, K. Hersvik and J. O. Fossum, *Nature communications*, 2013, **4**, 2066.

25 A. Kyrylyuk, A. Zvelindovsky, G. Sevink and J. Fraaije, *Macromolecules*, 2002, **35**, 1473–1476.

26 K. Lyakhova, A. Zvelindovsky and G. Sevink, *Macromolecules*, 2006, **39**, 3024–3037.

27 P. J. Flory, *The Journal of chemical physics*, 1942, **10**, 51–61.

28 M. L. Huggins, *The Journal of chemical physics*, 1941, **9**, 440–440.

29 M. Mittal, P. P. Lele, E. W. Kaler and E. M. Furst, *The Journal of chemical physics*, 2008, **129**, 064513.

30 D. Streeter and R. Boyer, *Industrial & Engineering Chemistry*, 1951, **43**, 1790–1797.

31 G. D. Phillies, *The Journal of Physical Chemistry*, 1989, **93**, 5029–5039.

32 K. Ngai and G. D. Phillies, *The Journal of chemical physics*, 1996, **105**, 8385–8397.

33 G. D. Phillies, *Macromolecules*, 1986, **19**, 2367–2376.

34 Paul Millett Research Group, *Meso Simulation Code*, `https://github.com/paulmillett/meso/tree/develop`.

35 L. Q. Chen and J. Shen, *Computer Physics Communications*, 1998, **108**, 147–158.

36 M. Frigo and S. G. Johnson, *Proceedings of the IEEE*, 2005, **93**, 216–231.

37 S. Frijters, T. Krüger and J. Harting, *Computer Physics Communications*, 2015, **189**, 92–98.

38 E. Herzig, K. White, A. Schofield, W. Poon and P. Clegg, *Nature materials*, 2007, **6**, 966.

39 H.-j. Chung, K. Ohno, T. Fukuda and R. J. Composto, *Nano letters*, 2005, **5**, 1878–1882.

40 S. Gam, A. Corlu, H.-J. Chung, K. Ohno, M. J. Hore and R. J. Composto, *Soft Matter*, 2011, **7**, 7262–7268.

41 L. Bai, J. W. Fruehwirth, X. Cheng and C. W. Macosko, *Soft Matter*, 2015, **11**, 5282–5293.

42 C. Park and R. E. Robertson, *Materials Science and Engineering: A*, 1998, **257**, 295–311.

43 M.-K. Schwarz, W. Bauhofer and K. Schulte, *Polymer*, 2002, **43**, 3079–3082.

44 H. Koerner, J. Jacobs, D. W. Tomlin, J. D. Busbee and R. Vaia, *Advanced Materials*, 2004, **16**, 297–302.

45 C. Martin, J. Sandler, A. Windle, M.-K. Schwarz, W. Bauhofer, K. Schulte and M. Shaffer, *Polymer*, 2005, **46**, 877–886.

46 Y. Guo, Y. Chen, E. Wang and M. Cakmak, *ACS applied materials & interfaces*, 2016, **9**, 919–929.

47 *Fused Silica — SiO2 Material Properties*, `http://accuratus.com/fused.html`, (Accessed on 04/20/2018).

48 S. Wada, H. Yasuno, T. Hoshina, S.-M. Nam, H. Kakemoto and T. Tsurumi, *Japanese journal of applied physics*, 2003, **42**, 6188.

49 H.-J. Chung, J. Kim, K. Ohno and R. J. Composto, *ACS Macro Letters*, 2011, **1**, 252–256.

50 G. Venugopal, S. Krause and G. Wnek, *Journal of Polymer Science Part C: Polymer Letters*, 1989, **27**, 497–501.

51 J. Serpico, G. Wnek, S. Krause, T. Smith, D. Luca and A. Van Laeken, *Macromolecules*, 1991, **24**, 6879–6881.

52 G. Venugopal and S. Krause, *Macromolecules*, 1992, **25**, 4626–4634.

53 G. Venugopal, S. Krause and G. E. Wnek, *Chemistry of Materials*, 1992, **4**, 1334–1343.

Table of Contents Graphic

Electric-field alignment of particle-stabilized emulsions within thin-film geometries enables through-thickness morphologies, revealed with mesoscopic computer simulations.